Optics and Lasers in Engineering 198 (2026) 109529

Contents lists available at ScienceDirect

Optics and Lasers in Engineering

journal homepage: www.elsevier.com/locate/optlaseng

Development of a cost-effective optical fiber non-contact object classification system using machine learning techniques

Şekip Esat Hayber [a,*], Serkan Keser [b], Yunus Görkem [c]

[a] Bursa Uludağ University, Department of Electrical-Electronics Engineering, Bursa, 16059, Türkiye
[b] Kırşehir Ahi Evran University, Department of Electrical-Electronics Engineering, Kırşehir, 40100, Türkiye
[c] Kırşehir Ahi Evran University, Kaman Vocational School, Department of Electricity and Energy, Kırşehir, 40360, Türkiye

ARTICLE INFO

Keywords:
Machine learning
Deep learning
Neural networks
Non-contact object classification
Photonics
Plastic optical fiber

ABSTRACT

Material-specific spectral reflectance provides a reliable basis for identification and classification. Based on this principle, we offer a low-cost, three-wavelength, distance-scanning fiber optic system that is ideal for material identification, surface defect inspection, and quality control in confined or difficult-to-access industrial settings. In this study, we developed a compact, cost-effective, optical fiber non-contact object classification (OF-NOC) using three distinct wavelengths. Reflectance data collected from ten objects is used to train and test various machine and deep learning classifiers, including a narrow-layered neural network (NL-NN), a bilayered NN (BL-NN), a trilayered NN (TL-NN), a weighted K-nearest neighbors (WKNN), a support vector machine (SVM), a convolutional neural network (CNN), a gated recurrent unit (GRU), and a long short-term memory (LSTM). The ten objects were restructured into four material-based classes to evaluate generalization performance. For ten objects, the GRU model achieved the highest average accuracy (0.939), followed closely by the TL-NN (0.919) and cubic SVM (0.913). The proposed OF-NOC system demonstrates strong classification performance and has advantages such as portability, scalability, and hardware simplicity. Thanks to its compact structure, low-cost design, and proven performance, the system provides a scalable solution for industrial quality control, robotic sensing, and precise object classification applications.

1. Introduction

Object classification has a wide range of applications, including materials characterization and the development of autonomous systems [1–3]. The accurate identification of surface features is crucial for classifying objects, which is essential for operational efficiency, safety, and quality control processes. Conventional surface detection methods have limitations regarding resolution, speed, and the ability to operate in harsh environmental conditions; hence, there is a need for more advanced methods and techniques [4,5].

In object identification processes, the structural properties of object surfaces are important. Determining surface properties is crucial in various sectors, including automotive [6], aerospace [7], manufacturing [8], healthcare [9,10], electronics [11], construction [12], energy [13,14], and agriculture [15].

Methods for analysing surface properties based on stylus-type [16], acoustic [17], thermal [18,19], and electrical [20–22] principles are available in the literature. These traditional approaches are generally categorized into two main types: contact and non-contact methods. Contact techniques provide high sensitivity but carry the risk of low measurement speed and surface damage/marking [16], while non-contact methods exhibit limitations in the resolution–speed–stability balance due to sensitivity to environmental variables, high cost, or the need for strict experimental control [20].

Fiber optic sensing can mitigate these limitations, offering advantages such as high sensitivity, immunity to electromagnetic interference, a compact and scalable architecture, and inherently non-contact operation. However, previous fiber optic studies have mostly relied on a single wavelength [23], required complex or specialised production setups [24], or relied on simple statistical feature processing for classification [25].

In Hu et al.'s work, which utilizes a deep convolutional neural network (CNN) to classify five cell types, accuracy decreases as the detection depth increases. The charge-coupled device (CCD) camera and opto-mechanical setup required to capture the images, along with the steps for recording and aligning them, add extra complexity and require

* Corresponding author.
E-mail address: sehayber@uludag.edu.tr (Ş.E. Hayber).

https://doi.org/10.1016/j.optlaseng.2025.109529
Received 18 June 2025; Received in revised form 1 November 2025; Accepted 2 December 2025
Available online 6 December 2025

higher precision for practical use [26]. Although various contactless object classification systems, including those using high-resolution laser scanning, hyperspectral imaging [27], and capacitive proximity sensors [21], show promising results, they generally require complex hardware, highly controlled environments, or detailed calibration procedures.

This study presents a design for an optical fiber non-contact object classification (OF-NOC) system that can analyze three different wavelengths. The low-cost system's optical hardware components include a light source emitting three wavelengths, a photodetector capable of sensing these wavelengths, and dual-row POFs. The electronic components consist of a driver circuit that controls the timing of the light sources and a data acquisition unit (DAU) that collects electrical signals from the detector and transfers them to a computer. The acquired data is then processed through feature extraction, which derives features from the time-dependent change in distance. Classification was carried out using machine learning (weighted K-nearest neighbors (WKNN), support vector machine (SVM)), deep learning (CNN, gated recurrent unit (GRU), and long short-term memory (LSTM)), and ANN methods (narrow-layered neural network (NL-NN), bilayered NN (BL-NN), trilayered NN (TL-NN)). GRU is known to produce successful results in classifying time series features [28,29]. Since time-dependent features were used in this study, GRU was employed alongside other classifiers and was found to achieve the highest accuracy rates in the testing phase. To provide a more comprehensive assessment of the classifiers' performance, metrics such as the F1 score and accuracy rate were calculated. This work presents a low-cost, contactless classification approach combining multi-wavelength fiber-optic reflectance measurement and machine learning-based decision models to address these gaps.

The following sections of the paper present the design and object classification of the OF-NOC system in Section II, materials and methods. Section III presents the experimental results and discussion. The subheadings of this section are data acquisition, feature extraction, and classification. Finally, the conclusions are given in Section IV.

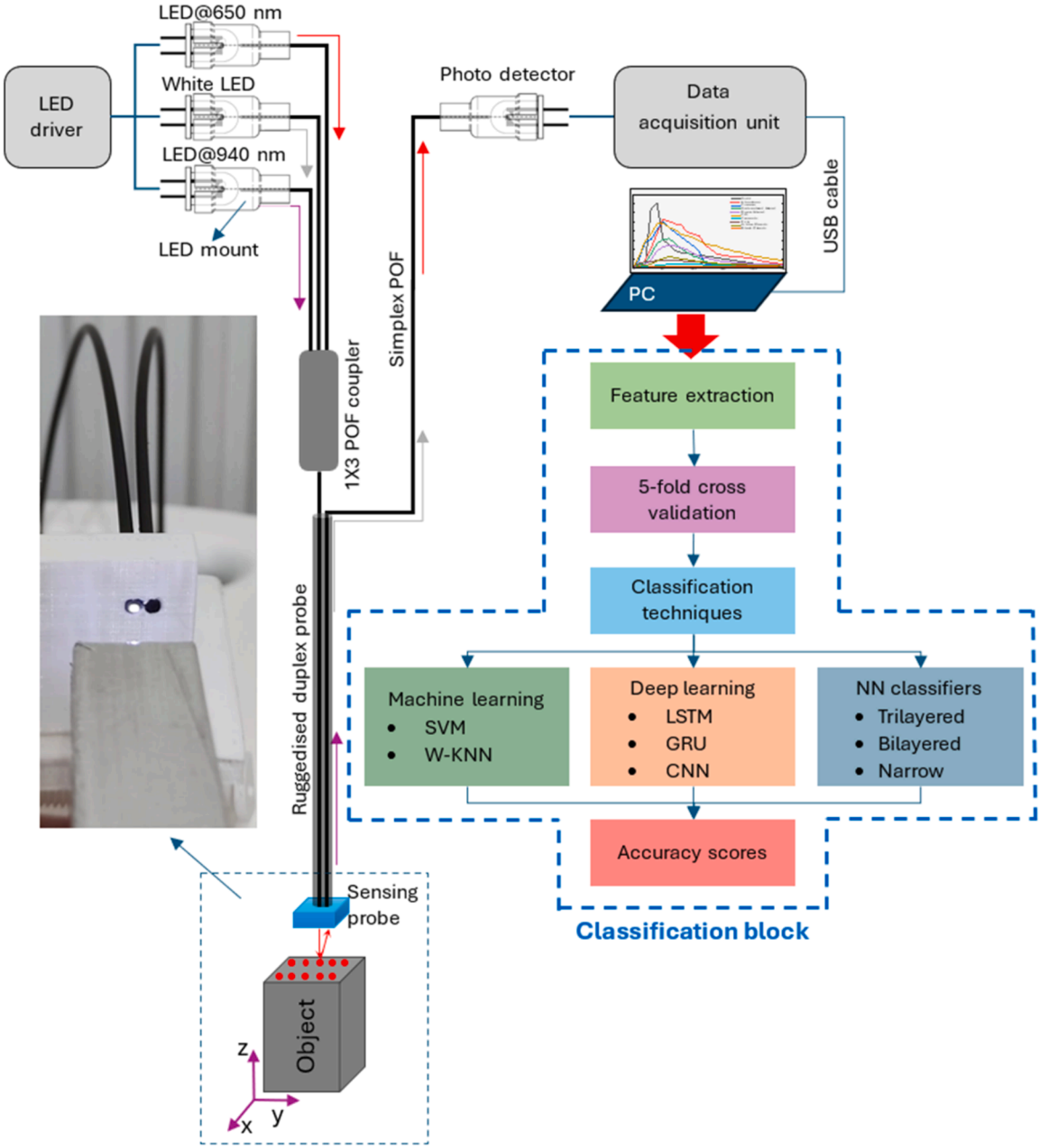

Fig. 1. OF-NOC system.

2. Materials and methods

2.1. Design of the OF-NOC system

Fig. 1 illustrates the schematic representation of the detection component of the OF-NOC system and the classification block. The diagram illustrates a line starting with an LED driver that sequentially powers three source outputs. These outputs are transmitted through a 1 × 3 plastic optic fiber (POF) coupler to a ruggedised duplex probe. The probe's transmitter fiber illuminates the surface, while the receiver simplex POF carries the reflected signal to the photodetector. Ten surface points are measured on each object, and at each point, the distance between the probe and the surface is scanned in 1 mm steps within a range of 1 to 25 mm. Consequently, voltage signals are sampled sequentially at three different wavelengths at each distance. The photodetector's output is then sampled by the DAU and transferred to the PC. The data is subsequently converted into six-dimensional feature vectors (three wavelength voltages, mean, standard deviation, and distance) on the PC using feature extraction. Five-fold cross-validation is applied to the feature vectors for testing. SVM, WKNN, CNN, LSTM, GRU, and various narrow, bilayered, and trilayered neural network classifiers are then comparatively trained. Performance metrics are reported using accuracy and F1 scores.

The sensing part of the system comprises an LED driver, three distinct-wavelength LEDs (650 nm GaAlAs red, 5000 mcd InGaN white, and 940 nm GaAlAs infrared) mounted to 5 mm (T1–3/4) LED–to–POF light pipes (2.2 mm OD), a 1 × 3 POF coupler (IF 543), and a simplex POF based on Mitsubishi GH4001 step-index optical fiber (1000 μm core, jacketed). The probe body was machined with two parallel 2.2 mm channels, and the fiber cables were inserted into these channels to form a rugged duplex sensing tip (separate transmit/receive paths). In the finalized bill of materials, three 5 mm LEDs were used: Vishay TLDR6800 (deep-red, 650 nm), Vishay VLHW5100 (white), and Vishay TSAL6100 (near-IR, 940 nm). The LEDs were housed in a VCC THR 5 22 LED-to-fiber connector, compatible with a 2.2 mm jacket POF, which fed the 1 × 3 POF coupler at the sensing end. Reflected light was detected by a 5 mm silicon PIN photodiode (Everlight PD333–3C/H0/L2; spectral band 400–1100 nm, peak sensitivity 940 nm) and routed via the simplex POF to the DAU input. The photodiode output was digitized using an ESP32 DevKitC interfaced to an ADS1115 16-bit ADC (I^2C; up to 860 S/s). Measurements used single-ended mode with PGA ±4.096 V; sampling at 800 S/s. The three LEDs were time-multiplexed with a 0.2 s dwell per wavelength (red→white→IR), and—for each window—the initial 50 ms was discarded for settling while the subsequent 150 ms segment was averaged to obtain a robust intensity estimate. All other hardware settings and processing steps were kept identical. A dark offset (LEDs off) was taken at the start of each run and subtracted from all readings. This procedure improves SNR without additional hardware filtering and ensures repeatability across objects and sessions. The red–white–IR triad provides complementary spectral responses over common engineering materials, while the photodiode's 940 nm peak enhances IR SNR. The U3-HV offers an inexpensive, USB-powered DAU with sufficient resolution and bandwidth for the low-frequency, time-multiplexed protocol, aligning with the system's low-cost, contactless design goals. For cost transparency, the probe bill of materials is approximately $87, excluding the DAU. With an ultra-low-cost ESP32+ADS1115 DAU, the end-to-end hardware cost is approximately $115–120 (or $247 with a LabJack U3-HV), based on typical online list prices at the time of purchase (excluding the PC). These figures are provided to substantiate the "cost-effective" claim while keeping all components vendor-agnostic.

The fundamental concept underlying the surface reflectance detection region of the OF-NOC system is a multimode fiber comprising two-step index profiles: one for transmitting light and the other for receiving light (Fig. 1). The source light intensity, $I(r,z)$, is expressed as a function of light intensity distribution, as detailed in (1) [30].

$$I(r,z) = \frac{P_E}{\pi w^2(z)} \exp\left(-\frac{2r^2}{w^2(z)}\right) \tag{1}$$

In this context, P_E represents the optical power emitted from the transmitting fiber, r denotes the radial coordinate, and z is the longitudinal coordinate. The beam radius, $w(z)$, is a function of the distance z and is defined by (2).

$$w(z) = w_0\sqrt{1+\left(\frac{z}{z_R}\right)^2} \tag{2}$$

In this context, the beam waist radius, w_0, is defined as the radius of the beam at its waist, and the Rayleigh distance, z_R, is given by (3).

$$z_R = \frac{\pi w_0^2}{\lambda} \tag{3}$$

The power $P(z)$ of the reflected light collected by the receiving fiber is evaluated by integrating the irradiance over the core area S of the receiving fiber, as outlined in (4) [31].

$$P(z) = \int_S I(r,z)dS \tag{4}$$

This expression constitutes the fundamental principle underlying the sensor's functionality for displacement detection. The sensor's sensitivity is contingent upon the parameters of the fiber, the fluctuations in the reflector's intensity, and the source's intensity.

2.2. Object classification

Before measurement, all surfaces of the ten objects were cleaned using a standardised 70 % isopropanol solution to remove grease and dust. The objects were then left to air dry to ensure consistent measurement conditions. Measurements were performed under normal conditions. The object sampling protocol involved collecting measurements from ten separate, randomly selected points on the surface of each object. These ten points were selected from an approximate 30 × 30 mm grid on the target surface to ensure that the 250 data points (ten points × 25 distances) captured representative intra-class variability across the planar area of the object, rather than relying on a single potential outlier.

In the study, the voltage values obtained at three distinct light wavelengths for ten different objects were determined with one-millimeter measurement intervals. For each wavelength, the values are obtained at 25 mm, resulting in 250 values (ten points × 25 distances) for each object. The total number of values accumulated for each wavelength is 2500. The values above are then combined in columns for the three specified wavelengths, resulting in a 2500 × 6 data matrix. The test process is conducted through the implementation of a five-fold cross-validation approach. The structure of the values in a row of 2500 × 6-dimensional features is illustrated in Fig. 2.

Fig. 2 illustrates that the initial value of the feature is the distance between 1 and 25 mm. The subsequent values represent the voltage measurements obtained under infrared, red, and white light. The mean and standard deviation values of the three voltage values are presented in the fifth and sixth columns, respectively. Furthermore, the five metallic, two plastic, and two ceramic object classes were combined separately and treated as three distinct classes. Four classes were identified, with the remaining courses situated outside the three classes. The 2500 × 6 dataset was classified after being updated according to the labels of these four classes. This second classification method aimed to examine the classification performance of objects with similar properties. The study presents the best results from the numerous hyperparameters tested for the classifiers. These results are stated in the classifier descriptions.

Furthermore, the ten individual object classes were intentionally

Distances (mm)	Infrared (V)	Red (V)	White (V)	The mean of voltages	The standard deviation of voltages

Fig. 2. Structure of the feature.

combined into four broader, material-based classes. This strategic merging aimed to address one of the study's primary objectives: testing the system's robustness and ability to generalize when classifying objects by their material type (e.g., metallic, plastic) rather than specific object identity. The four resulting classes were metallic (gold, aluminum, copper, galvanized steel, rose metal), highly reflective (mirror), ceramic (ceramic 1, ceramic 2), and plastic (PVC plastic, black plastic). This secondary classification approach offers valuable insight into the system's usefulness for industrial and robotic applications, where recognizing material types generally takes precedence over individual object differentiation.

The study used a classification learner application in MATLAB for classification with WKNN, SVM, and three NN classifiers [32,33]. The application allows training and testing models for data classification using supervised machine learning methods. Furthermore, classification was conducted by implementing LSTM, GRU, and CNN code in MATLAB. The classifier structures employed in the study are outlined in the following section.

WKNN represents a modified K nearest neighbor's algorithm version, as outlined in reference [34]. One factor that impacts the efficacy of the KNN algorithm is the selection of the hyperparameter K. If K is insufficiently large, the algorithm will be more susceptible to outliers. Conversely, if K is huge, the neighborhood may encompass a disproportionate number of points from other classes. The traditional KNN and WKNN algorithms utilize the spatial distance between the reference points and the test point to select the K nearest reference points. Euclidean and Manhattan distances are the most employed spatial distances [35,36]. The KNN algorithm selects the K reference regions with the smallest spatial distances. The reference points' average values (x_T, y_T) are calculated as the coordinates of the test points, as per the specifications of (5).

$$(x_T,\ y_T) = \frac{\sum_{i=1}^{K}(x_i,\ y_i)}{K} \tag{5}$$

In the WKNN algorithm, the K reference points with the smallest spatial distances are selected utilizing a weighted average. Given that the distances of the selected reference points to the test point are disparate, the weights assigned to the reference points are also variable. The weights of the selected reference points can be calculated by (6), wherein the weight is inversely proportional to the spatial distance d_{iT}. The WKNN algorithm attains superior positioning accuracy relative to the KNN algorithm and is the most prevalent matching algorithm [37]. In the study, the nearest neighbour method with $K = 5$ and the Euclidean (L2) norm were used to measure distance. Additionally, the contribution of each neighbour was weighted inversely to its distance (distance weighting (inverse)).

$$w_{iT} = \frac{\frac{1}{d_{iT}}}{\sum_{i=1}^{K}\frac{1}{d_{iT}}} \tag{6}$$

The coordinates of the test point (x_T,y_T) are calculated by (7):

$$(x_T,\ y_T) = \sum_{i=1}^{K} w_{iT}(x_i,\ y_i) \tag{7}$$

In (5) and (7), (x_i,y_i) are the coordinates of the reference points.

SVM classification is achieved by identifying the optimal hyperplane that separates data points belonging to a given class from those belonging to a different class [38]. In the context of SVM, the optimal hyperplane is defined as the hyperplane with the most significant margin between the two classes [39]. In this study, the cubic and quadratic kernels are employed (C-SVM, Q-SVM). A standard box constraint was used for regularisation within two different SVM kernels. The kernel function of the cubic SVM (C-SVM) classifier is provided in (8).

$$k(x_i, x_j) = \left(x_i^T x_j\right)^3 \tag{8}$$

Fig. 3 shows an example of classification using the SVM kernel. LSTM, a recurrent neural network (RNN), is a type of deep learning architecture that employs previous data to enhance the network's performance on present and upcoming inputs [40]. An LSTM network is a specific form of RNN designed to capture and learn long-term dependencies within sequential data [41]. The LSTM block diagram employed for classification is illustrated in Fig. 4.

In the study, 200 neurons were utilized in the hidden layer for the LSTM model. The number of epochs was set to 2000, with 20 mini-batches generated for each epoch. LSTM has a hidden layer, an adaptive moment estimation (Adam) optimizer, a learning rate of 0.001, and a dropout rate of 0.2. Fig. 5 illustrates the structure of the LSTM cell employed in the study. The LSTM cell comprises four components: the input gate (i), the forget gate (f), the cell candidate (g), and the output gate (o). The LSTM layer comprises learnable parameters, including the input weights W, the recurrent weights R, and the bias b. Each matrix, W, R, and b, comprises the respective input weights, recurrent weights, and bias for the different gates [42]. As illustrated in (9), the matrices are concatenated.

$$\begin{aligned} W &= \begin{bmatrix} W_i & W_f & W_g & W_o \end{bmatrix},\ R = \begin{bmatrix} R_i & R_f & R_g & R_o \end{bmatrix},\ b \\ &= \begin{bmatrix} b_i & b_f & b_g & b_o \end{bmatrix} \end{aligned} \tag{9}$$

Where i, f, g, and o represent the input, forget, cell candidate, and output gates, respectively. The cell state at any given time t can be described by:

$$c_t = f_t \odot c_{t-1} + i_t \odot g_t \tag{10}$$

Where $\odot$ is the Hadamard product. The hidden state at time step t is represented as:

$$d_t = o_t \odot \eta_c(c_t) \tag{11}$$

η_c denotes the cell activation function, typically computed using the hyperbolic tangent function. The gate states of the LSTM unit at time t can be detailed as follows using (12):

$$\begin{aligned} i_t &= \eta_g(W_i x_t + R_i d_{t-1} + b_i) \\ f_t &= \eta_g(W_f x_t + R_f d_{t-1} + b_f) \\ g_t &= \eta_c(W_g x_t + R_g d_{t-1} + b_g) \\ o_t &= \eta_g(W_o x_t + R_o d_{t-1} + b_o) \end{aligned} \tag{12}$$

Where η_g and η_c represent the activation functions for the gates and the cell state, respectively.

In this study, three different NN architectures were utilized: NL-NN, BL-NN, and TL-NN. These NN's consist of an input layer, fully connected (FC) layers, the rectified linear unit (ReLU) activation function, a softmax layer for classification, and an output layer that contains the predicted class labels. The TL-NN has three hidden layers with 64, 32, and 16 neurons, respectively. The BL-NN has two hidden layers with 64 and 32 neurons, respectively. The NL-NN has one hidden layer with 32 neurons. The softmax layer has as many outputs as the number of classes, and test data is classified based on the probability values obtained from the softmax function [43]. In all the NN architectures, the FC layers have ten outputs, except for the final FC layer, which has M outputs corresponding to the number of classes. The softmax function is

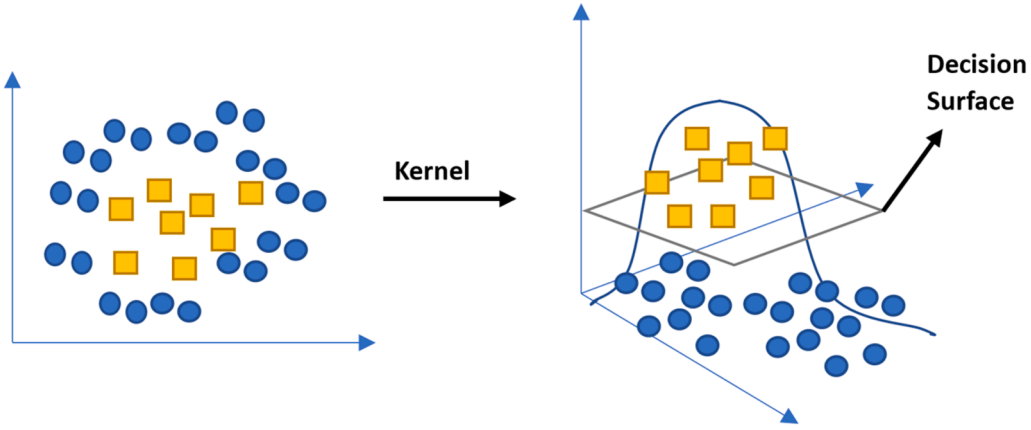

Fig. 3. A classification example with an SVM kernel.

Fig. 4. The proposed LSTM algorithm structure.

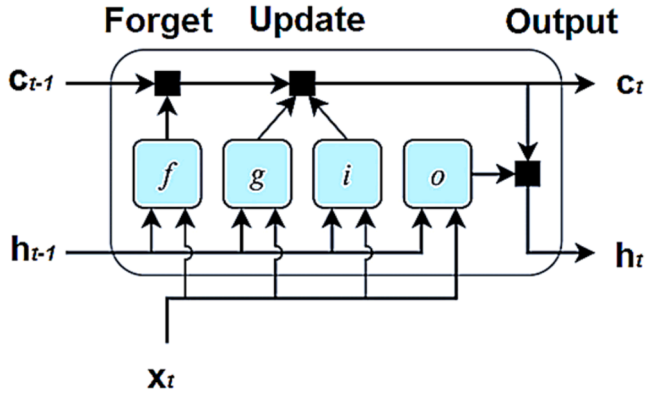

Fig. 5. The structure of an LSTM cell.

applied to the final fully connected layer. This function takes each input x_i and performs the following transformation:

$$f(x_i) = \frac{e^{x_i}}{\sum_{j=1}^{M} e^{x_j}} \tag{13}$$

M represents the total number of classes, and the outputs correspond to the predicted classification probabilities. The output layer provides the predicted class labels. Fig. 6 illustrates the structural configurations of the three NN classifiers employed in the study.

CNNs have become the standard tool for various tasks, including image classification, object detection, and segmentation, due to their ability to learn hierarchical feature representations directly from data [44,45]. In this study, CNN training was performed using input values prepared for classification. The CNN structure is presented in Fig. 7. The number of epochs for the CNN was 3500, and the mini-batch size was 16. The data is treated as a one-dimensional vector. The convolutional layer applies a one-dimensional convolution operation. Features are extracted from the input using filters of size 3×1. Sixteen filters are used, which means the layer will produce 16 feature maps as output. The ReLU layer applies a nonlinear activation function to the data obtained after convolution. The max pooling layer reduces the dimensions of the feature maps, lowering computational cost while preserving essential

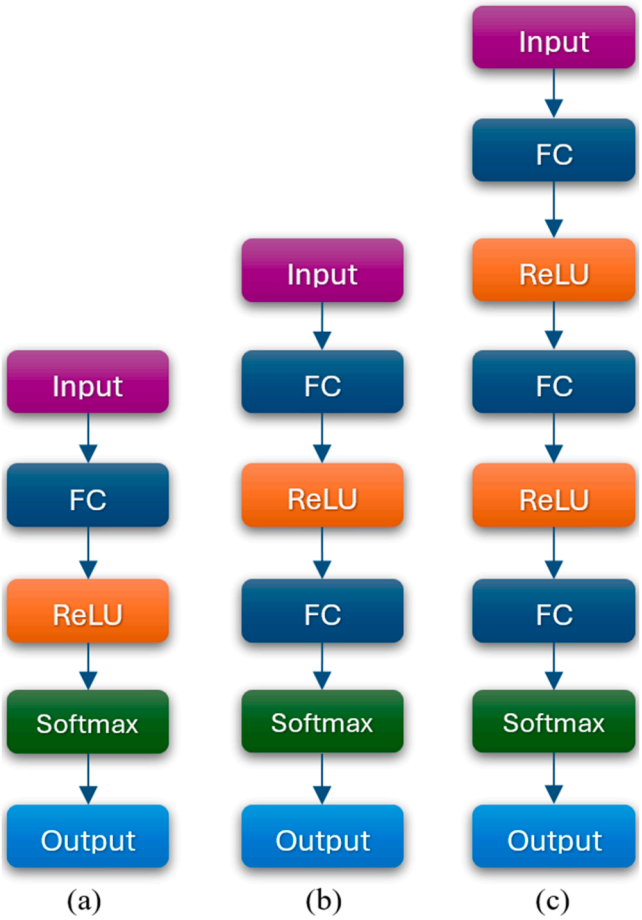

Fig. 6. Structures of (a) the NL-NN, (b) the BL-NN, and (c) the TL-NN.

features. A pooling window of size 2×1 slides across the feature map, selecting the maximum value. The fully connected layer takes the outputs from the convolutional layers. The number of outputs in this layer

Fig. 7. Proposed CNN structure.

equals the number of classes. The softmax layer generates probability scores for each class, normalizing the outputs so that their sum equals 1. The classification layer, the model's final layer, selects the class with the highest probability score based on the output from the softmax layer.

GRU is a cell type developed to solve the vanishing gradient problem of RNN and offers a more straightforward and less parameterized structure as an alternative to LSTM [46]. In the study, the epoch number for GRU was selected as 2800, and the mini-batch number was chosen as 16. The GRU structure used in the study is given in Fig. 8. The GRU layer processes the model's input layer data. GRU has a hidden layer (100 neurons), an Adam optimizer, a learning rate of 0.001, and a dropout of 0.2. One hundred units indicate the number of cells in the layer, and "Output: Last" means that the state at the end of the output sequence is taken. This layer is used to model long-term dependencies in sequential data. The fully connected layer is a classical NN layer in which each neuron is connected to all neurons in the previous layer. This layer receives the output from the GRU layer and forwards it to the required number of neurons for classification. The softmax layer produces probability scores for each class of the model. These scores are normalized to sum to 1, thus determining which class is the most probable. The classification layer selects the class with the highest probability using the probability distribution from the softmax layer.

2.3. Hyperparameter selection

The key hyperparameters listed in Table 1 were determined using 5-fold grid search for SVM, K and weighting in WKNN based on the local smoothness assumption, in GRU/LSTM, based on the dependency structure of the 25-step distance sequence and the dataset size for the number of hidden units/layers/dropout; in CNN, the kernel size/number of filters was selected to capture short-range patterns on the distance axis; and in NNs, the model capacity was limited to avoid overfitting. The key hyperparameters in Table 1 are the parameters that yielded the best test results. For the GRU model, 100 hidden units were used to balance model capacity and computational complexity. A mini-batch size of 16 and 2800 epochs provided sufficient convergence without overfitting. For the LSTM model, 200 hidden neurons and 2000 epochs were chosen based on their effectiveness in similar time-series classification tasks [40]. The CNN model employed 16 filters of size 3×1 in the convolutional layer, a standard kernel size in one-dimensional signal processing, with 3500 epochs to ensure stability in validation accuracy. For the NN architectures (NL-NN, BL-NN, TL-NN), fully connected layers with 10 neurons were used, followed by a softmax layer with the same number of output classes, as is widely applied in multi-class classification [43].

Three variants of NN architectures were designed: NL-NN, BL-NN, and TL-NN. They differ in the number of hidden layers and neurons. The TL-NN includes three hidden layers with 64, 32, and 16 neurons, respectively. This configuration was chosen to balance model complexity and generalization, based on performance observed during validation. The cubic and quadratic kernel types for SVM were selected after preliminary tests showed better performance than linear kernels, particularly for nonlinear separability [38,39]. $K = 5$ was used for the WKNN classifier, which provided a balance between sensitivity to noise and generalization [35,37]. All models were trained using 5-fold cross-validation to ensure generalizability and to avoid overfitting. These hyperparameter choices are summarized in Table 1, along with the rationale for their selection.

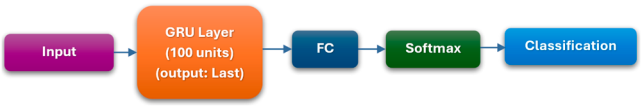

Fig. 8. Proposed GRU structure.

Table 1
Hyperparameter selection.

Model	Key Hyperparameters	Selection Rationale
TL-NN	3 hidden layers (64–32–16 neurons), ReLU, softmax	Balanced complexity and performance; validated through preliminary tests
BL-NN	2 hidden layers (64–32 neurons), ReLU, softmax	Reduced model size with acceptable accuracy; reference to similar works
NL-NN	1 hidden layer (32 neurons), ReLU, softmax	Simplified network for baseline comparison
C-SVM	Cubic kernel, standard box constraint	Best performance in validation among linear and quadratic kernels
Q-SVM	Quadratic kernel, standard box constraint	Tested for comparison, but lower performance than cubic
WKNN	$K = 5$, distance weighting (inverse), Euclidean	Standard K value; inverse weighting gives better generalization
CNN	1 conv layers, filter size=3×1, 16 filters, 1 FC layer, dropout=0.2	Effective for low-dimensional data; common design in similar studies
GRU	1 GRU layer (100 units), dropout=0.2, Adam, LR=0.001	Performs well in temporal data; stable convergence in trials
LSTM	1 LSTM layer (200 units), dropout=0.2, Adam, LR=0.001	Captures long-term dependencies; typical architecture in literature

3. Experimental results and discussion

3.1. Data acquisition

The images of the objects to be classified within the scope of this study are shown in Fig. 9. This study utilized a dataset collected from ten objects selected to represent various spectral reflectance profiles. The set contained five metallic objects: gold (polished plate), aluminium (brushed coating, Al-6061 alloy), copper (electrolytic grade), galvanized steel (zinc-coated, matte finish), and rose metal (bismuth alloy). The remaining five objects exhibited various non-metallic and complex reflective properties: a highly reflective mirror surface, ceramic-1 (glazed with a white coating), ceramic-2 (off-white, unglazed coating), PVC plastic (white, textured coating), and black plastic (matte black coating). To isolate the spectral reflection properties of the materials from geometric distortion, all measurements were consistently taken from planar areas.

In our study, light beams of three wavelengths, 650 nm GaAlAs red, 940 nm GaAlAs infrared, and 5000 mcd InGaN white, were incident on surfaces with different reflectance values via fibers. The light beams reflected from the surfaces were collected using the receiver fiber. While performing these operations, the transmitter and collector fiber pair were pulled back to 25 mm with 1 mm step intervals, starting from a point very close to the surface to be recognized (1 mm), and 25 measurements were taken. Similarly, measurements were taken at ten points on the target object's surface, and 250 data points were collected for each target object. During the data acquisition, 250 samples were collected for each target object by recording responses at 25 different distances and 10 surface points. This multi-point sampling approach was designed to capture intra-class variability due to minor surface irregularities, positioning errors, and reflection inconsistencies, thereby

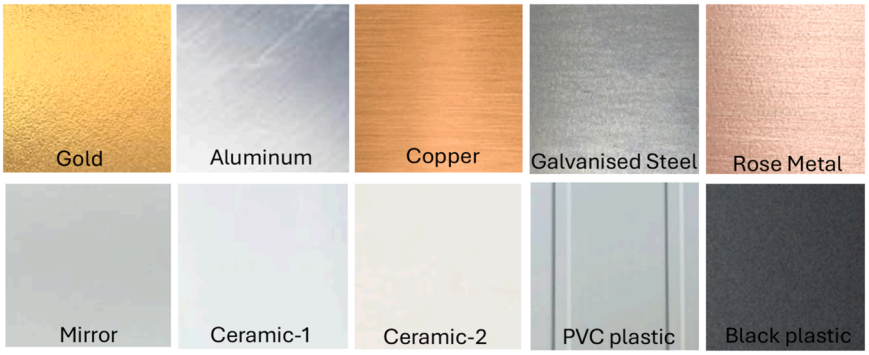

Fig. 9. The objects.

enhancing dataset robustness. While augmenting the dataset size has generally enhanced model generalization, collecting 2500 samples across 10 classes was deemed adequate to attain stable accuracy rates during 5-fold cross-validation. During this time, changes in light intensity on the detector, to which the collector fiber was connected, were observed depending on the incidence and reflection angles. These changes were converted into meaningful voltage values and recorded. Differences in the signals received for each surface were observed in the multiple experiments. These changes are shown in Fig. 10.

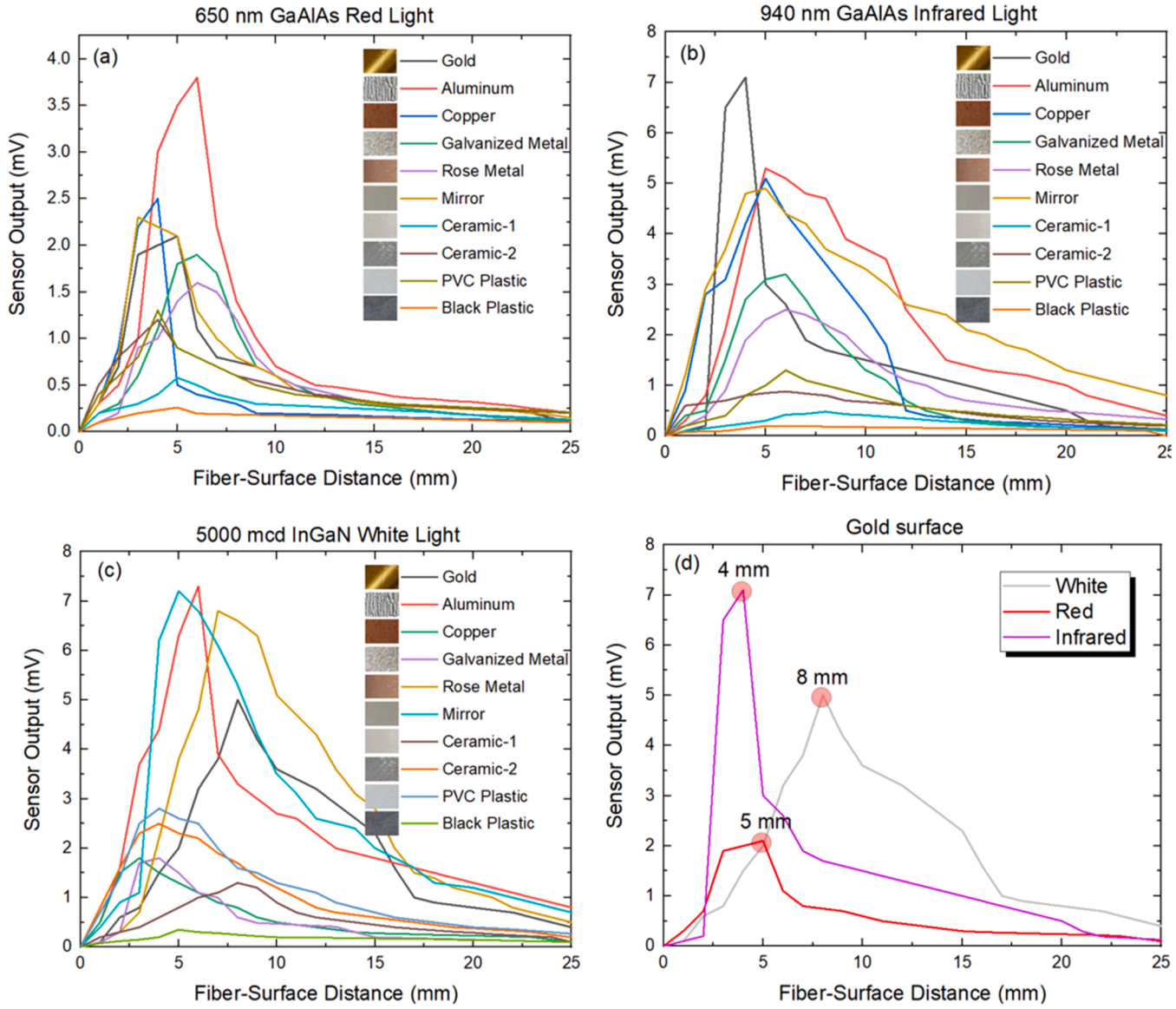

Fig. 10. The target objects are reacted to by three different wavelengths of sensor output after measurement: (a) 650 nm, (b) 940 nm, (c) white light, and (d) gold surface.

3.2. Feature extraction

The light rays reflected from the target surface were transmitted to the photodetector via the receiver fiber, and signal outputs were obtained. Initially, a 1 mm distance was maintained between the object and the fiber ends. By changing the distance between the probe tip and the target surface, the responses of each object under three different light characteristics and at different measurement distances were recorded by DAU and transferred to the PC via USB, thanks to the changes in the detector output voltage caused by the changes in the amplitude of the light. For each 1 mm distance interval, three voltage values were recorded in a file using the surface responses of three different wavelengths, created by the code written in the MATLAB environment on the PC. To minimize measurement errors that may occur due to surface roughness of the objects, measurements were taken at 10 different points on each object. Then, the distance between the object and the fiber probe was increased by 1 mm, and this process was repeated. This process continues for each object until the distance between the sensing probe and the object is 25 mm. Thus, a dataset of 250 lines, consisting of three voltage values, is obtained for each object. A total of 2500 lines of data are created for ten objects. In addition to the voltage values in the classification phase, the average, standard deviation, and distance to the object of the three voltage values are also added as features. Thus, a six-dimensional feature vector is obtained. The 2000 $\times$ 6 part of the obtained 2500 $\times$ 6-dimensional feature matrix was used as training, and the 500 $\times$ 6 part as testing. Minimal preprocessing was applied to the raw sensor data before model training. All voltage measurements were normalized to a 0–1 range using min-max scaling to ensure scale consistency across the three distinct wavelengths. Since the experimental setup was designed to minimize external light interference and electrical noise, no significant outliers or noise artifacts were observed in the collected data. Consequently, no additional filtering, smoothing, or complex feature extraction techniques were necessary. The high quality of the raw measurements allowed the classifiers to achieve stable performance using directly normalized features. While no advanced preprocessing was required under the controlled laboratory conditions of this study, future work involving larger or more complex datasets or operations in noisier environments may incorporate additional preprocessing techniques, such as noise reduction, data augmentation, or dimensionality reduction, to further enhance model robustness. The separation into training and testing parts was done with 5-fold cross-validation. The study classified objects using three different NN structures: deep learning algorithms GRU, CNN, and LSTM, and machine learning algorithms SVM and KNN.

3.3. Classification

This study evaluated nine different classification algorithms to assess system performance. We implemented the deep learning models via custom MATLAB scripts and trained the CNN and classical machine learning models using MATLAB's Classification Learner App. Model performance was assessed using accuracy and F1-score metrics for a stable evaluation. Since the dataset exhibited mild class instability (see Table 2), the F1 score was particularly useful for capturing performance consistency across all classes. Initially, the dataset comprised ten objects, which were grouped into four classes based on material characteristics: five metallic objects (Class 1), one mirror object (Class 2), two ceramic objects (Class 3), and two plastic objects (Class 4). Table 2 summarizes the distribution of training and test samples for these merged classes.

Table 2
Several samples of new classes were formed by merging classes.

Sample numbers	Class 1	Class 2	Class 3	Class 4
Total	1250	250	500	500
Training	1000	200	400	400
Test	250	50	100	100

Tables 3 and 4 summarize the accuracy and F1 values found using five-fold cross-validation for nine classifiers in both ten- and four-class scenarios. In the ten-class case (Table 3), GRU led with an accuracy of 0.939, followed by the TL-NN (0.919), the C-SVM (0.913), and LSTM (0.910). In the four-class configuration (Table 4), GRU again achieved the highest accuracy (0.946), with the TL-NN (0.929), C-SVM (0.928), and LSTM (0.921) close behind. In contrast, several algorithms exhibited inferior performance consistently across both classification scenarios. The WKNN algorithm produced the lowest accuracies and F1 scores, likely due to its sensitivity to class overlaps and limited ability to model nonlinear relationships in multi-wavelength reflectance data. Similarly, while the Q-SVM slightly outperformed the WKNN, it struggled with generalizing to complex class boundaries due to kernel limitations. Limited to a single hidden layer, the NL-NN demonstrated insufficient capacity to learn complex patterns, resulting in lower classification metrics. Overall, the results highlight the benefits of models that capture complex feature relationships (e.g., a TL-NN) or sequential temporal patterns (e.g., GRU). This is especially true in scenarios involving time-dependent and multidimensional sensor data. Fig. 11 depicts the average classification performance for ten-class and four-class structures. Under identical training settings (Adam, learning rate, batch size, and early stopping), the GRU converged faster than the LSTM and reached a similar validation plateau with a smaller train–validation gap. We attribute this to the GRU's simpler gating (reset/update) and lower parameterization, which better match the short, multi-distance dependencies of our 25-step sequences; the LSTM's higher capacity required more iterations and showed a slightly stronger tendency toward overfitting, explaining the GRU's superior mean validation accuracy (0.939). Reducing the labels from ten objects to four material families (defined a priori in Sec. II.B) improves accuracy and F1, consistent with increased inter-class margins under material-level grouping.

Fig. 11(a) shows the confusion matrix for the 0.926 accuracy achieved with the GRU in test no. 5, as presented in Table 3. Fig. 11(b) presents the confusion matrix for the 0.942 accuracy with GRU for the four classes in test no. 4, as shown in Table 4. Fig. 11(c) shows the confusion matrix for the 0.916 accuracy obtained with TL-NN in test no. 3 in Table 4.

Fig. 12(a) and Fig. 12(b) show the average accuracy and F1 values of the classifiers for Tables 3 and 4, respectively. In the ten-class scenario, the classifiers with the highest average performance are GRU (Acc = 0.939, F1 = 0.938), TL-NN (Acc = 0.919, F1 = 0.920), and C-SVM (Acc = 0.913, F1 = 0.914). The remaining classifiers, ranked in order of decreasing accuracy, include LSTM, CNN, BL-NN, NL-NN, Q-SVM, and WKNN. When the number of classes drops to four, most classifiers show a notable increase in performance. The top accuracies in this case are achieved by GRU, TL-NN, LSTM, CNN, BL-NN, NL-NN, Q-SVM, and WKNN, respectively. The strong alignment between F1 values and accuracy indicates a good balance between precision and recall, implying minimal impact of class imbalance. Overall, the ranking remains consistent across both scenarios, with GRU performing the best, while TL-NN and C-SVM serve as strong alternatives.

Fig. 13 illustrates the training performance of the LSTM model. Validation accuracy increases rapidly during the first 1000 iterations (to 0.80) and then rises more slowly, plateauing around 0.90–0.92 after 8000 iterations, while the cross-entropy decreases monotonically and levels off near 0.25–0.30. The shaded bands indicate the decreasing variance across folds, evidencing stable convergence. A small but persistent training–validation gap near convergence (training 0.98–0.99 vs. validation 0.91) suggests mild overfitting, which was mitigated by dropout and early stopping. Overall, the LSTM achieves acceptable generalization but remains below the GRU (0.939), likely because the GRU's lower parameterization and gating are better matched to the short, distance-driven dependencies of our 25-step sequences, whereas

Table 3
Accuracy and F1 values for ten classes.

Test no	TL- NN		BL-NN		NL-NN		C-SVM		Q-SVM		WKNN		CNN		GRU		LSTM	
	Acc.	F1	Acc.	F1	Acc.	F1	Acc.	F1	Acc.	F1	Acc.	F1	Acc.	F1	Acc.	F1	Acc.	F1
1	0.926	0.924	0.902	0.906	0.900	0.904	0.918	0.922	0.908	0.906	0.864	0.862	0.926	0.932	0.942	0.948	0.914	0.922
2	0.924	0.928	0.914	0.916	0.882	0.884	0.922	0.918	0.910	0.912	0.848	0.850	0.858	0.862	0.936	0.932	0.906	0.912
3	0.912	0.910	0.908	0.904	0.896	0.892	0.916	0.918	0.884	0.892	0.882	0.884	0.908	0.914	0.954	0.952	0.924	0.928
4	0.928	0.930	0.902	0.900	0.904	0.902	0.922	0.918	0.868	0.872	0.876	0.872	0.892	0.898	0.938	0.942	0.896	0.900
5	0.906	0.908	0.886	0.888	0.876	0.878	0.888	0.892	0.862	0.858	0.852	0.854	0.916	0.922	0.926	0.918	0.912	0.914
mean	**0.919**	**0.920**	**0.902**	**0.903**	**0.891**	**0.892**	**0.913**	**0.914**	**0.886**	**0.888**	**0.864**	**0.864**	**0.900**	**0.906**	**0.939**	**0.938**	**0.910**	**0.915**

Table 4
Accuracy and F1 values for four classes.

Test no	TL- NN		BL-NN		NL-NN		C-SVM		Q-SVM		WKNN		CNN		GRU		LSTM	
	Acc.	F1	Acc.	F1	Acc.	F1	Acc.	F1	Acc.	F1	Acc.	F1	Acc.	F1	Acc.	F1	Acc.	F1
1	0.926	0.924	0.904	0.902	0.896	0.902	0.938	0.940	0.896	0.892	0.868	0.870	0.908	0.912	0.942	0.940	0.928	0.930
2	0.932	0.930	0.916	0.918	0.884	0.886	0.930	0.934	0.884	0.880	0.844	0.848	0.912	0.910	0.944	0.950	0.922	0.926
3	0.916	0.922	0.902	0.904	0.900	0.896	0.908	0.912	0.868	0.872	0.898	0.902	0.924	0.928	0.956	0.940	0.936	0.934
4	0.938	0.936	0.922	0.926	0.916	0.912	0.924	0.928	0.888	0.892	0.866	0.872	0.916	0.924	0.942	0.942	0.916	0.918
5	0.936	0.932	0.906	0.908	0.894	0.896	0.942	0.940	0.876	0.878	0.836	0.842	0.896	0.902	0.946	0.944	0.904	0.900
mean	**0.929**	**0.929**	**0.910**	**0.912**	**0.898**	**0.898**	**0.928**	**0.931**	**0.882**	**0.883**	**0.862**	**0.867**	**0.911**	**0.915**	**0.946**	**0.943**	**0.921**	**0.922**

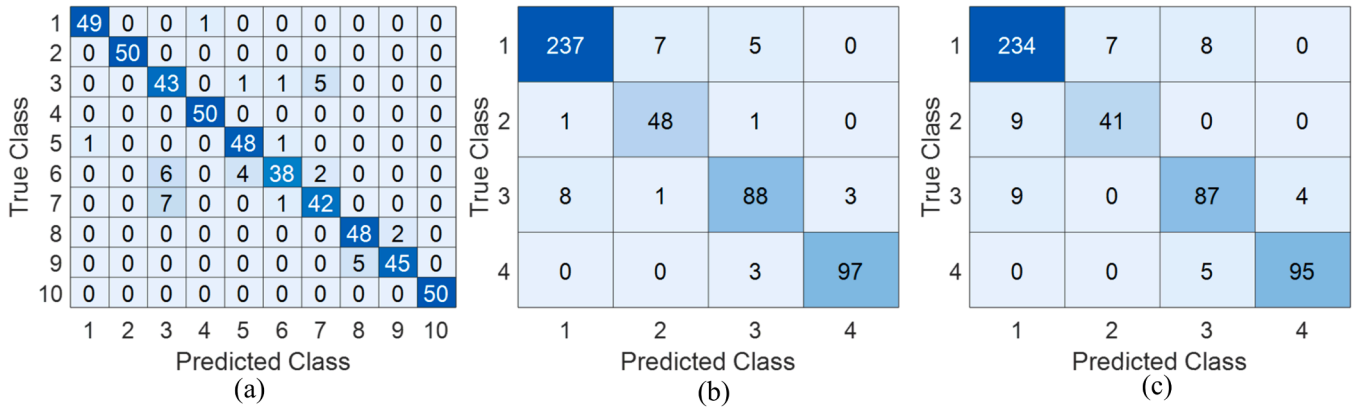

Fig. 11. Confusion matrices: (a) GRU (ten-class), (b) GRU (four-class), (c) TL-NN (four-class) test results.

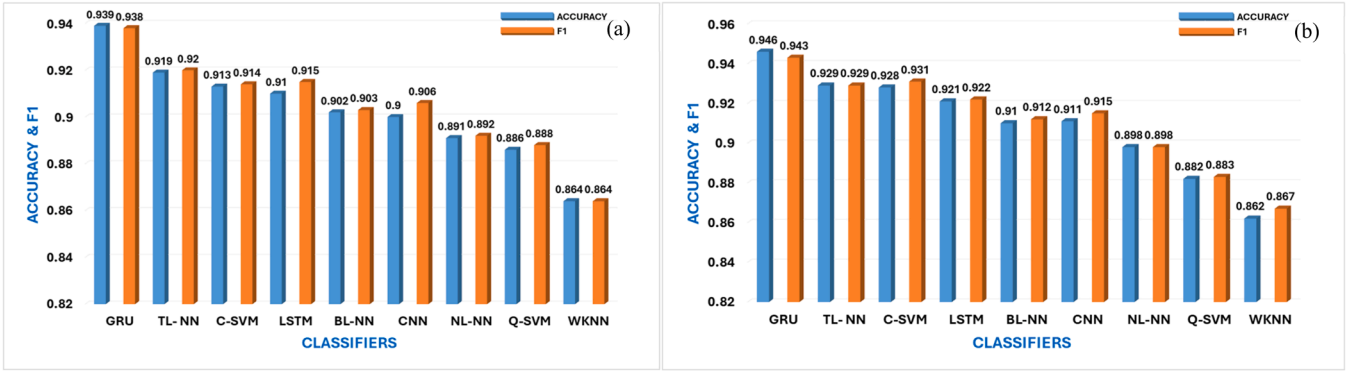

Fig. 12. Average accuracy and F1 values for (a) ten and, (b) four classes.

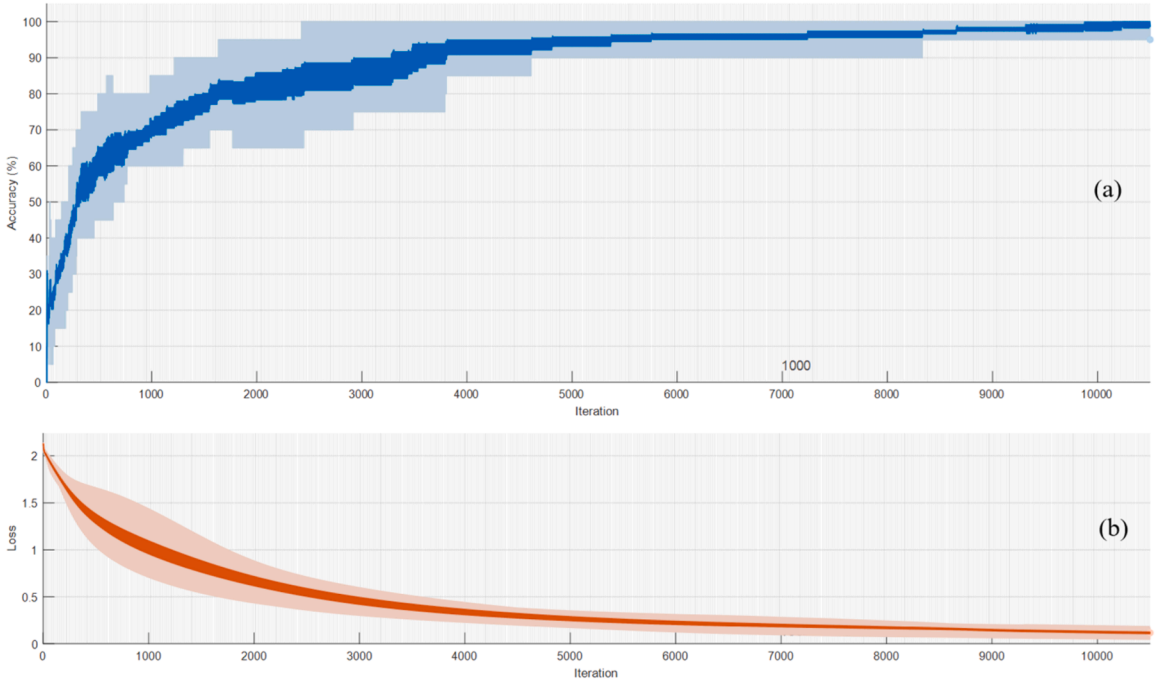

Fig. 13. (a) Accuracy rate and (b) loss (cross-entropy) function for LSTM.

the LSTM's higher capacity slows convergence and is more prone to overfitting under the available data volume.

A comparative evaluation of the proposed OF-NOC system against previous non-contact material recognition studies is summarized in Table 5. In Hu et al.'s study, Anderson-localizing glass-air optical fibers were combined with deep convolutional neural networks (DCNNs) to

Table 5
Literature comparison.

Studies	Technology used	Accuracy	Cost	Feasibility	Description
[47]	Plastic optical fiber, displacement, and single-wavelength color sensing (780 nm laser)	~0.85	Low	High	Single-wavelength POF displacement/color-contrast sensing on a small color set; simple hardware, no multi-wavelength modeling.
[23]	Optical reflectance fiber sensor	~0.88	Medium	Medium	Reflectance sensing configured for dental enamel stain detection; domain-specific optics and dataset.
[26]	Glass-air Anderson localization fiber, deep CNN	0.912	Medium-High	Medium	Bending-insensitive speckle recognition with GALOF and deep CNN; specialized fiber fabrication.
This study	Plastic optical fiber, 3-wavelength LED, GRU	0.939	Low	High	Tri-wavelength POF reflectance with distance sweep; 10-class evaluation (metals/non-metals); GRU accuracy 0.939; compact, low-cost probe.

classify microscopic biological objects directly from speckle patterns, thereby eliminating the need for explicit image reconstruction [26]. Although their system achieved respectable classification accuracy (0.912), its fabrication complexity, fiber cost, and experimental setup are considerably higher than the compact, low-cost OF-NOC structure. Azri et al. [47] report a POF-based color-sensing system that explicitly emphasizes low production cost and practical design, utilizing a single-wavelength displacement configuration on a small set of color targets. The study does not model multi-wavelength reflectance or evaluate multi-material scenarios. Rahman et al. [23] describe an intensity-modulated POF setup for dentistry that is "simple in design and low in cost," tailored to dental enamel stain detection with domain-specific geometry and materials. By contrast, Hu et al. [26] employ a glass-air Anderson localizing fiber (GALOF) fabricated via the stack-and-draw method, which utilizes microscope objectives and a CCD camera, thereby increasing component/fabrication demands, as well as setup complexity. In this context, our OF-NOC uses three wavelengths with a systematic distance sweep and evaluates 10 classes (metals and non-metals), achieving a mean validation accuracy of 0.939 with a GRU classifier, while maintaining a compact, low-cost fiber-probe form factor suitable for confined-space deployment.

However, their system lacks the general-purpose, multi-material versatility demonstrated by the OF-NOC system. In contrast, the OF-NOC system presented in this study achieves superior performance. It achieves an accuracy of 0.939, even under a more challenging ten-class scenario, using only low-cost plastic optical fibers and easily accessible multi-wavelength LED sources. Furthermore, integrating GRU-based temporal deep learning models significantly enhances classification stability across varying distances and multidimensional feature spaces. The compactness, portability, and low energy requirements of the OF-NOC system provide strong advantages for scalable, real-time applications.

The experimental findings consistently demonstrate the effectiveness and robustness of the proposed multi-wavelength, fiber-optic, non-contact object classification system when applied to various material types, class structures, and time-dependent measurement scenarios. Throughout the analysis, the GRU-based model consistently outperformed other models, achieving an average accuracy of 0.939 in the ten-class configuration. This is primarily due to the GRU's ability to model temporal dependencies and dynamic patterns in multi-wavelength reflectance profiles acquired at various distances from the target surface. As each voltage measurement reflects a sequential, distance-dependent sampling structure, the GRU's recurrent architecture successfully captures these evolving reflectance dynamics. The TL-NN classifier also yielded successful results. Similarly, the C-SVM classifier performed with high stability, successfully generating the complex nonlinear decision boundaries necessary to distinguish subtle differences between material categories. In contrast, example-based classifiers such as KNN and WKNN performed poorly, particularly in higher-class settings. Specifically, when the classification task was reformulated by combining ten material classes into four groups, accuracy improved across all classifiers. This reflects the natural tendency of similar material types to cluster, and shows that reducing intra-class heterogeneity makes it easier to define boundaries, enabling more consistent model convergence, even with traditional machine learning algorithms. The system's design could offer significant practical advantages beyond classification accuracy in various application areas. Its lightweight, low-cost, compact fiber-optic probe structure makes it ideal for robotic platforms. It could facilitate real-time material recognition for adaptive manipulation, intelligent sorting, and safe interaction with heterogeneous environments. In industrial production lines, for example, the system could be used as a rapid, non-contact quality control tool to assess surface quality, coating uniformity, and post-processing surface integrity, and it could operate robustly under challenging conditions such as heat, vibration, and particle exposure. For this technology to be applicable in the field of biomedicine, further development is required in terms of biocompatibility, sterilisation protocols, and seamless integration with existing clinical workflows. From a broader perspective, the experimental results confirm the strong correlation between the data collection strategy and the classification algorithm capabilities. The repetitive modelling capability of GRU, the deep representation power of TL-NN, and the margin maximisation efficiency of SVM collectively demonstrate the feasibility of achieving highly accurate material classification using multi-wavelength surface reflectance data.

5. Conclusions

This work introduces a novel, cost-effective OF-NOC system based on a sensor structure that detects light at three different wavelengths. Experimental validation confirmed the system's performance using low-cost plastic optical fibers and readily available LED sources, supporting its cost-effectiveness (See Section II.A). In the ten-class material identification task, the GRU classifier achieved the highest average accuracy of 0.939, which increased to 0.946 when materials were grouped into four broader classes (Tables 3 and 4). These accuracy results reflect the consistent performance obtained from the 5-fold cross-validation process. The system shows potential to address key limitations noted in previous fiber optic classification research, which was often limited by single-wavelength detection and reliance on simple, manually crafted features. GRU achieved the best average accuracy by effectively capturing short-distance dependencies in multi-wavelength data through a sequential multi-distance reflection model. TL-NN and C-SVM models also achieved top accuracy rates after GRU.

TL-NN efficiently learns complex, nonlinear interactions between wavelength and distance features, while C-SVM provides the benefit of high accuracy and low computational cost. In contrast, classifiers such as KNN and WKNN have struggled to model sequential, high-dimensional data without a dedicated feature learning mechanism.

The main advancement of this work is in the design and integration of sequential deep learning with multispectral data. This provides a practical approach to achieving high-accuracy object classification, overcoming previous complexity and cost issues. The compact POF probe design is particularly suitable for inspections in tight spaces and for easy integration with robots. Future work will aim to expand the range of materials and distances, explore additional optimal wavelengths, and advance embedded applications to enhance the system's robustness and operational capabilities.

CRediT authorship contribution statement

Şekip Esat Hayber: Writing – review & editing, Writing – original draft, Validation, Supervision. **Serkan Keser:** Writing – original draft, Software, Data curation. **Yunus Görkem:** Writing – original draft, Validation, Resources, Methodology.

Declaration of competing interest

The authors declare that they have no known competing financial interests or personal relationships that could have appeared to influence the work reported in this paper.

Acknowledgment

The infrastructure and facilities of the Optics Laboratory (Department of Electrical and Electronics Engineering, Bursa Uludağ University) were used in this research, supported by Project FPDD-2025–2230.

Data availability

Data will be made available on request.

References

[1] Chen Y, Ding Y, Zhao F, Zhang E, Wu Z, Shao L. Surface defect detection methods for industrial products: a review. Appl Sci 2021;11(16):7657. https://doi.org/10.3390/app11167657.
[2] Liu G. Surface defect detection methods based on deep learning: a brief review. In: In 2020, the 2nd International Conference on Information Technology and Computer Application (ITCA). IEEE; 2020. p. 200–3. https://doi.org/10.1109/ITCA52113.2020.00049.
[3] Ibrahim AAM, Tapamo JR. A survey of vision-based methods for surface defects' Detection and classification in steel products. In Inform 2024;11(2):25. https://doi.org/10.3390/informatics11020025. MDPI.
[4] Liu Y, Zhang C, Dong X. A survey of real-time surface defect inspection methods based on deep learning. Artif Intell Rev 2023;56(10):12131–70. https://doi.org/10.1007/s10462-023-10475-7.
[5] Wang K, Zhou T, Li X, Ren F. Performance and challenges of 3D object detection methods in complex scenes for autonomous driving. IEEE Trans Intell Veh 2022;8(2):1699–716. https://doi.org/10.1109/TIV.2022.3213796.
[6] Yogeswaran A, Payeur P. 3d surface analysis for automated detection of deformations on automotive body panels. New Adv Veh Technol Automot Eng 2012. https://doi.org/10.5772/45790. 978-953.
[7] Peltier F, Thierry D. Review of Cr-free coatings for the corrosion protection of aluminum aerospace alloys. Coatings 2022;12(4):518. https://doi.org/10.3390/coatings12040518.
[8] Sushmna A. Steps involved in quality control and inspection of CNC machining. Violintec 2024. https://www.violintec.com/precision-machining/steps-involved-in-quality-control-and-inspection-of-cnc-machining/.
[9] Chen Z, Lee JB. Biocompatibility of su-8 and its biomedical device applications. Micromachines 2021;12(7):794. https://doi.org/10.3390/mi12070794.
[10] Al-Zyoud W, Haddadin D, Hasan SA, Jaradat H, Kanoun O. Biocompatibility testing for implants: a novel tool for selection and characterization. Materials 2023;16(21):6881. https://doi.org/10.3390/ma16216881.
[11] Wang W, Sun L, Wang G, Zhang P, Qi L, Zheng L, Dong W. The effect of sample surface roughness on the microanalysis of microchip laser-induced breakdown spectroscopy. J Anal Spectrom 2020;35(2):357–65. https://doi.org/10.1039/C9JA00377K.
[12] Thissen P, Bogner A, Dehn F. Surface treatments on concrete: an overview on organic, inorganic and nano-based coatings and an outlook about surface modification by rare-earth oxides. RSC Sustain 2024. https://doi.org/10.1039/D3SU00482A.
[13] Scholtz L, Ladanyi L, Mullerova J. Influence of surface roughness on optical characteristics of multilayer solar cells. Adv Electr Electron Eng 2015;12(6):631–8. https://doi.org/10.15598/aeee.v12i6.1078.
[14] Farshad FF, Rieke HH. Gas well optimization: a surface roughness approach. In: In SPE Unconventional Resources Conference/Gas Technology Symposium. SPE; 2008. SPE–114486. https://doi.org/10.2118/114486-MS.
[15] Abdulraheem MI, Zhang W, Li S, Moshayedi AJ, Farooque AA, Hu J. Advancement of remote sensing for soil measurements and applications: a comprehensive review. Sustainability 2023;15(21):15444. https://doi.org/10.3390/su152115444.
[16] Adamczak S, Świderski J, Stępień K, Dobrowolski T, Chmielik I. Comparative analysis of surface roughness measurements obtained with the use of contact stylus profilometry and coherence scanning interferometry. In: In XXI IMEKO World Congress "Measurement in Research and Industry; 2015. p. 1560.
[17] Kurşun K, Güven F, Ersoy H. Utilizing piezo acoustic sensors for the identification of surface roughness and textures. Sensors 2022;22(12):4381. https://doi.org/10.3390/s22124381.
[18] De Maddis M, Lunetto V, Razza V, Russo Spena P. Infrared thermography for investigation of surface quality in dry finish turning of Ti6Al4V. Metals 2022;12(1):154. https://doi.org/10.3390/met12010154.
[19] Rost E, Hecker C, Schodlok MC, Van der Meer FD. Rock sample surface preparation influences thermal infrared spectra. Minerals 2018;8(11):475. https://doi.org/10.3390/min8110475.
[20] Kinnunen K, Tiainen T, Viitala R. The effect of surface roughness variations to eddy current displacement measurement. In: In 2023 IEEE International Instrumentation and Measurement Technology Conference (I2MTC). IEEE; 2023. p. 1–6. https://doi.org/10.1109/I2MTC53148.2023.10175923.
[21] Wang HL, Chen T, Zhang B, Wang G, Yang X, Wu K, Wang Y. A dual-responsive artificial skin for tactile and touchless interfaces. Small 2023;19(21):2206830. https://doi.org/10.1002/smll.202206830.
[22] Alshawabkeh M, Alagi H, Navarro SE, Duriez C, Hein B, Zangl H, Faller LM. Highly stretchable additively manufactured capacitive proximity and tactile sensors for soft robotic systems. IEEE Trans Instrum Meas 2023;72:1–10. https://doi.org/10.1109/TIM.2023.3250232.
[23] Rahman HA, Rahim HRA, Harun SW, Yasin M, Apsari R, Ahmad H, Abas WW. Detection of stain formation on teeth by oral antiseptic solution using fiber optic displacement sensor. Opt Laser Technol 2013;45:336–41. https://doi.org/10.1016/j.optlastec.2012.06.027.
[24] Acharya A, Kawade N. A Fabry–Perot interferometer-based fiber optic dynamic displacement sensor with an analog in-phase/quadrature generator. IEEE Sens J 2020;20(24):14764–71. https://doi.org/10.1109/JSEN.2020.3009587.
[25] Nan-Nan Z, Jun Z. Surface roughness measurement based on fiber optic sensor. Measurement 2016;86:239–45. https://doi.org/10.1016/j.measurement.2016.02.051.
[26] Hu X, Zhao J, Antonio-Lopez JE, Fan S, Correa RA, Schülzgen A. Robust imaging-free object recognition through anderson localizing optical fiber. J Light Technol 2020;39(4):920–6. https://doi.org/10.1109/JLT.2020.3029416.
[27] Bezák T, Kusý M, Eliáš M, Kopček M. Surface roughness determination using laser scanning confocal microscope Zeiss LSM 700. In: In Proc. 22nd Int. Conf. Metallurgy Mater.(METAL); 2013. p. 1–6.
[28] Zhu H, Zhang J, Cui H, Wang K, Tang Q. TCRAN: multivariate time series classification using residual channel attention networks with time correction. Appl Soft Comput 2022;114:108117. https://doi.org/10.1016/j.asoc.2021.108117.
[29] Zhao H, Chen Z, Jiang H, Jing W, Sun L, Feng M. Evaluation of three deep learning models for early crop classification using sentinel-1A imagery time series—a case study in Zhanjiang. China Remote Sens 2019;11(22):2673. https://doi.org/10.3390/rs11222673.
[30] Zubia G, Zubía J, Amorebieta J, Aldabaldetreku G, Durana G. A new method to design trifurcated optical fiber displacement sensors. IEEE Sens J 2023. https://doi.org/10.1109/JSEN.2023.3337311.
[31] Harun SW, Yang HZ, Yasin M, Ahmad H. Theoretical and experimental study on the fiber optic displacement sensor with two receiving fibers. Microw Opt Technol Lett 2010;52(2):373–5. https://doi.org/10.1002/mop.24900.
[32] Peng Z, Wen H, Jian J, Gribok A, Wang M, Huang S, Chen KP. Identifications and classifications of human locomotion using Rayleigh-enhanced distributed fiber acoustic sensors with deep neural networks. Sci Rep 2020;10(1):21014. https://doi.org/10.1038/s41598-020-77147-2.
[33] Silva CN, Lopes FF, Matos JA, Castro MCF. Arrythmia classification using MATLAB® classification Learner app. Biosignals 2023:220–5. https://doi.org/10.5220/0011666300003414.
[34] Gou J, Du L, Zhang Y, Xiong T. A new distance-weighted k-nearest neighbor classifier. J Inf Comput Sci 2012;9(6):1429–36.
[35] Zuo W, Zhang D, Wang K. On kernel difference-weighted k-nearest neighbor classification. Pattern Anal Appl 2008;11:247–57. https://doi.org/10.1007/s10044-007-0100-z.
[36] Gou J, Xiong T, Kuang Y. A novel weighted voting for K-nearest neighbor rule. J Comput 2011;6(5):833–40. https://doi.org/10.4304/jcp.6.5.833-840.
[37] Gao Y, Gao F. Edited AdaBoost by weighted kNN. Neurocomputing 2010;73(16–18):3079–88. https://doi.org/10.1016/j.neucom.2010.06.024.
[38] Amarappa S, Sathyanarayana SV. Data classification using Support vector Machine (SVM), a simplified approach. Int J Electron Comput Sci Eng 2014;3:435–45.
[39] Bhavsar H, Panchal MH. A review on support vector machine for data classification. Int J Adv Res Comput Eng Technol 2012;1(10):185–9.
[40] Apaydin H, Feizi H, Sattari MT, Colak MS, Shamshirband S, Chau KW. Comparative analysis of recurrent neural network architectures for reservoir inflow forecasting. Water 2020;12(5):1500. https://doi.org/10.3390/w12051500.
[41] Tan K, Wang D. A convolutional recurrent neural network for real-time speech enhancement. Interspeech 2018;2018:3229–33. https://doi.org/10.21437/Interspeech.2018-1405.
[42] Curreri F, Patanè L, Xibilia MG. RNN-and LSTM-based soft sensors transferability for an industrial process. Sensors 2021;21(3):823. https://doi.org/10.3390/s21030823.
[43] Amin J, Anjum MA, Malik M. Fused information of DeepLabv3+ and transfer learning model for semantic segmentation and rich features selection using equilibrium optimizer (EO) for classification of NPDR lesions. Knowl Based Syst 2022;249:108881. https://doi.org/10.1016/j.knosys.2022.108881.
[44] Krizhevsky A, Sutskever I, Hinton GE. Imagenet classification with deep convolutional neural networks. Adv Neural Inf Process Syst 2012;25.

[45] Li Z, Liu F, Yang W, Peng S, Zhou J. A survey of convolutional neural networks: analysis, applications, and prospects. IEEE Trans Neural Netw Learn Syst 2021;33 (12):6999–7019. https://doi.org/10.1109/TNNLS.2021.3084827.
[46] Chung, J., Gulcehre, C., Cho, K., & Bengio, Y. (2014). Empirical evaluation of gated recurrent neural networks on sequence modeling. arXiv preprint https://doi.org/10.48550/arXiv.1412.3555.
[47] Azri MFM, Zulkifli MZ, Muhammad FD, Yusof MK, Bahari MS, Samsudin SA, Yasin M. Color detection using non-target reflectivity plastic optical fiber displacement sensor. Microw Opt Technol Lett 2020;62(11):3640–4. https://doi.org/10.1002/mop.32472.

Şekip Esat Hayber received his BSc degree at Mersin University in 2004, his MSc in 2014, and his PhD at Erciyes University in 2018. All of the degrees are in the field of Electrical and Electronics Engineering. Hayber is currently an Assoc. Professor at Bursa Uludağ University Faculty of Engineering, Electrical and Electronics Engineering. His research involves optical and fiber optic detection, optical fiber sensing systems, and photonic sensors, and he also works on system energy efficiency. For more detailed information, you can visit https://www.sehayber.com.

Serkan Keser received an MSc and a Ph.D. in Electrical-Electronics Engineering from Eskişehir Osmangazi University in 2008 and 2018, respectively. He is working as an Assoc. Professor at the Department of Electrical and Electronics Engineering, Kırşehir Ahi Evran University. His current research interests are signal and systems, digital signal processing, speech and image recognition, signal coding, and artificial neural networks.

Yunus Görkem received the MSc degree from the Institute of Advanced Technologies, Kırşehir Ahi Evran University, Kırşehir, Türkiye, in 2022. He is currently working as a Lecturer with the Department of Electrical and Energy, Kırsehir Ahi Evran University, Kırşehir, Türkiye. His research interests include optical and fiber-optic detection, optical fiber sensing systems, and photonic sensors.